Advances in Materials Research, *Vol. 15, No. 2 (2026) 167-186*
https://doi.org/10.12989/amr.2026.15.2.167

Techno-Press

Management of thermal buckling and stability in auxetic hybrid nanocomposite annular plates

Anwar Ahmed*

Department of Civil Engineering, College of Engineering, Northern Border University, Arar 73222, Arar, Saudi Arabia

(Received October 21, 2025, Revised March 7, 2026, Accepted April 16, 2026)

Abstract. This research provides a broad management-oriented inquiry into the thermal buckling and stability behavior of hybrid nanocomposite-strengthened annular plates inside an auxetic elastic medium. The structural arrangement is treated via a multi-scale hybrid laminated nanocomposite (MHLN) scheme together with a higher-order shear deformation theory (HSDT) so it can properly catch the transverse shear effect and those thickness-dependent changes. Thermoelastic stress–strain relations are used too to see how thermal loading nudges the nonlinear stability properties of the ring-like layout. On top of that, the nearby auxetic substrate is modeled with the Haber–Schaim elastic foundation approach, which helps in a more realistic sense of how the negative Poisson's ratio actually boosts stiffness and also how it improves post-buckling resistance. The governing equilibrium equations are discretized and handled numerically by using the differential quadrature method (DQM) built on a Chebyshev–Gauss–Lobatto grid distribution, which gives strong computational efficiency and reliable numerical convergence. Parametric studies are then run to look at how foundation coefficients, temperature changes, nanoparticle dispersion, lamination sequence, and geometric ratios influence the critical buckling temperatures and overall structural stability. What comes out is a useful management scaffold for best design choices, thermal reliability checking, and stability regulation of advanced nanocomposite plate structures, for aerospace, mechanical, and energy engineering use cases.

Keywords: auxetic elastic foundation; HSDT; management; MHLN; thermal buckling stability

1. Introduction

Nanocomposite reinforcement has become an important area of research in modern materials science because it improves the mechanical, thermal, and electrical properties of materials [1, 2]. Nanocomposites are materials that contain nanoparticles dispersed within a matrix such as polymers, metals, or ceramics [3]. The addition of nanoscale reinforcements significantly enhances the strength and durability of the base material [4]. These reinforcements can include carbon nanotubes, graphene, nanoclays, and metal oxide nanoparticles [5]. Due to their extremely small size, nanoparticles provide a large surface area for interaction with the matrix material [6]. This strong interfacial bonding improves load transfer and increases the overall performance of the composite [7]. Nanocomposite reinforcement is widely used in aerospace industries to produce lightweight yet strong structural components [8]. In the automotive sector, reinforced nanocomposites

*Corresponding author, Ph.D., E-mail: Anwar.ahmed@nbu.edu.sa

http://www.techno-press.org/amr/5

ISSN: 2234-0912 (Print), 2234-179X (Online)

help reduce vehicle weight and improve fuel efficiency [9]. The construction industry also benefits from nanocomposites because they enhance crack resistance and structural stability [10]. In electronics, nanocomposite materials improve conductivity and thermal management capabilities [11]. Biomedical applications use reinforced nanocomposites for implants, drug delivery systems, and tissue engineering [12]. The excellent corrosion resistance of nanocomposites makes them suitable for harsh environmental conditions [13]. Nanocomposite reinforcement also improves wear resistance, leading to longer service life of engineering components [14]. Researchers continue to explore eco-friendly nanocomposites for sustainable material development [15]. The use of nanotechnology in reinforcement allows the production of multifunctional materials with superior performance [16]. These materials can simultaneously provide strength, flexibility, and thermal stability [17]. Nanocomposite reinforcement contributes to energy savings by reducing material consumption and improving efficiency [18]. Advanced manufacturing techniques have made the production of nanocomposites more reliable and cost-effective [19]. Despite some challenges related to uniform nanoparticle dispersion, continuous research is overcoming these limitations [20]. Overall, nanocomposite reinforcement plays a crucial role in advancing modern engineering and industrial applications [21].

Shear deformation theories are important in engineering because they provide more accurate predictions of the behavior of beams, plates, and composite structures [22]. Classical theories often neglect transverse shear effects, which can lead to errors in thick structural elements [23]. Shear deformation theories help engineers analyze stresses and deflections more precisely under different loading conditions [24]. These theories are widely used in aerospace, civil, mechanical, and marine engineering applications [25]. They improve the design of modern lightweight structures made from composite and sandwich materials [26]. By considering shear effects, engineers can enhance structural safety and reliability [27]. Shear deformation theories also contribute to optimizing material usage and reducing structural weight [28].

The present research develops an advanced analytical framework for the management and control of thermal buckling phenomena in annular plates reinforced with hybrid nanocomposite laminates and supported by an auxetic elastic foundation. A multi-scale hybrid laminated nanocomposite (MHLN) model is adopted to characterize the effective mechanical behavior of nano-reinforced layers across different material scales. The structural formulation is established using higher-order shear deformation theory, which accurately accounts for transverse shear deformation without requiring shear correction factors. Thermoelastic stress–strain constitutive relations are incorporated to investigate the coupled influence of thermal loading and elastic constraints on structural stability. In addition, the surrounding medium is modeled through the Haber–Schaim auxetic elastic foundation model to capture the stiffness modulation and enhanced energy absorption associated with negative Poisson's ratio materials. The resulting governing equations are solved numerically using the differential quadrature method implemented with Chebyshev–Gauss–Lobatto grid points, providing improved computational precision and convergence characteristics. A comprehensive parametric study evaluates the effects of temperature rise, nanoparticle volume fraction, boundary conditions, geometric parameters, and auxetic foundation coefficients on the critical thermal buckling response. The obtained results establish a reliable management strategy for optimizing structural resilience, enhancing thermal stability, and improving the safe performance of nanocomposite annular plate systems in high-temperature engineering environments.

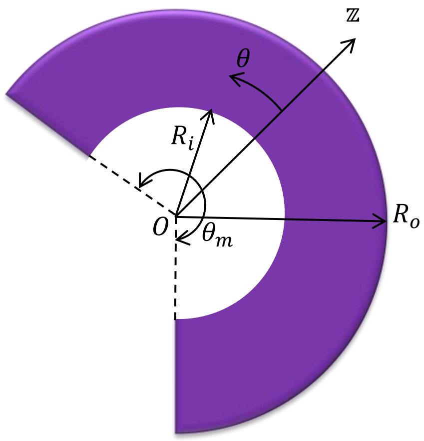

Figure 1. The geometrical configuration and mechanical modeling of a hybrid nanocomposite annular plate resting on an auxetic elastic foundation

2. Basic formulation

Fig. 1 has illustrated the geometrical configuration and mechanical modeling of a hybrid nanocomposite annular plate resting on an auxetic elastic foundation. The upper schematic has represented the thickness distribution and coordinate system of the plate–foundation assembly, where h denotes the plate thickness and h_f corresponds to the thickness of the auxetic foundation layer. The radial coordinate $\mathbb{r}$ and transverse coordinate $\mathbb{z}$ have defined the cylindrical coordinate system employed in the mathematical formulation. The spring-based representation with stiffness parameter K_w has modeled the elastic reaction of the auxetic foundation according to the Haber–Schaim foundation theory. This configuration has enabled the investigation of thermo-mechanical interactions between the nanocomposite plate and the surrounding elastic medium. The lower schematic has depicted the annular sector geometry of the plate. The structure has been characterized by the inner radius R_i and outer radius R_o, while θ has denoted the circumferential coordinate. The angular extent of the annular sector has been defined through the sector angle θ_m. The origin O has represented the center of curvature of the annular geometry. This mathematical model has provided the fundamental basis for deriving the governing equations of thermal buckling and stability using higher-order shear deformation theory and differential quadrature discretization techniques.

A two-step process is employed for the homogenization procedure, relying on both the Halpin-Tsai model [29] and a micromechanical formulation [30]. To begin, we determine the equivalent material properties of the composite, as shown in Ref. [31].

$$\mathbb{e}_{11} = \mathbb{v}_{\mathbb{F}}\mathbb{e}_{11}^{\mathbb{F}} + \mathbb{v}_{NCM}\mathbb{e}^{NCM}, \tag{1a}$$

$$\frac{1}{\mathbb{e}_{22}} = \frac{\mathbb{v}_{\mathbb{F}}}{\mathbb{e}_{22}^{\mathbb{F}}} + \frac{\mathbb{v}_{NCM}}{\mathbb{e}^{NCM}} - \mathbb{v}_{\mathbb{F}}\mathbb{v}_{NCM} \times \frac{\frac{(\nu^{\mathbb{F}})^2\mathbb{e}^{NCM}}{\mathbb{e}_{22}^{\mathbb{F}}} + \frac{(\nu^{NCM})^2\mathbb{e}_{22}^{\mathbb{F}}}{\mathbb{e}^{M}} - 2\nu^{\mathbb{F}}\nu^{NCM}}{\mathbb{v}_{\mathbb{F}}\mathbb{e}_{22}^{\mathbb{F}} + \mathbb{v}_{NCM}\mathbb{e}^{NCM}}, \tag{1b}$$

$$\mathbb{e}_{33} = \mathbb{e}_{22}, \tag{1c}$$

$$\frac{1}{\mathbb{G}_{12}} = \frac{\mathbb{v}_{\mathbb{F}}}{\mathbb{G}_{12}^{\mathbb{F}}} + \frac{\mathbb{v}_{NCM}}{\mathbb{G}^{NCM}}, \mathbb{G}_{23} = \mathbb{G}_{12}, \mathbb{G}_{13} = \mathbb{G}_{12}, \tag{1d}$$

$$\rho = \mathbb{v}_{\mathbb{F}} \rho^{\mathbb{F}} + \mathbb{v}_{NCM} \rho^{NCM}, \tag{1e}$$

$$\nu_{12} = \mathbb{v}_{\mathbb{F}} \nu^{\mathbb{F}} + \mathbb{v}_{NCM} \nu^{NCM}, \tag{1f}$$

$$\nu_{21} = \frac{\mathbb{e}_{22}}{\mathbb{e}_{11}} \nu_{12}, \qquad \nu_{13} = \nu_{12}, \qquad \nu_{31} = \nu_{21}, \qquad \nu_{32} = \nu_{21}, \qquad \nu_{23} = \nu_{32} \tag{1g}$$

The link connecting the two volume fractions is expressed in the following manner [31].

$$\mathbb{v}_{\mathbb{F}} + \mathbb{v}_{NCM} = 1, \tag{2}$$

In the next step, we determine the overall behavior of the CNT-reinforced nano-composite matrix by applying an extended version of the Halpin-Tsai micromechanical approach, following the procedure given in Ref. [32].

$$\mathbb{e}^{NCM} = \mathbb{e}^{M}\left(\frac{5}{8}\left(\frac{1 + 2\beta_{dd}\mathbb{v}_{CNT}}{1 - \beta_{dd}\mathbb{v}_{CNT}}\right) + \frac{3}{8}\left(\frac{1 + 2(l^{CNT}/d^{CNT})\beta_{dl}\mathbb{v}_{CNT}}{1 - \beta_{dl}\mathbb{v}_{CNT}}\right)\right) \tag{3}$$

In this context, the parameters β_{dd} and β_{dl} are obtained using the formula given below

$$\beta_{dl} = \frac{(\mathbb{e}_{11}^{CNT}/\mathbb{e}^{M}) - (d^{CNT}/4t^{CNT})}{(\mathbb{e}_{11}^{CNT}/\mathbb{e}^{M}) + (l^{CNT}/2t^{CNT})}, \quad \beta_{dd} = \frac{(\mathbb{e}_{11}^{CNT}/\mathbb{e}^{M}) - (d^{CNT}/4t^{CNT})}{(\mathbb{e}_{11}^{CNT}/\mathbb{e}^{M}) + (d^{CNT}/2t^{CNT})} \tag{4}$$

Given the value of W_{CNT}, one can write the expression for the CNT volume fraction in the following manner [29].

$$\mathbb{v}_{CNT}^{*} = \frac{W_{CNT}}{W_{CNT} + \left(\frac{\rho^{CNT}}{\rho^{M}}\right)(1 - W_{CNT})} \tag{5}$$

The through-thickness variation of the MHLN pattern takes the following form:

$$\mathbb{v}_{CNT} = \mathbb{v}_{CNT}^{*} \tag{6}$$

Moreover, the link between the two volume fractions is given by the expression below [33]:

$$\mathbb{v}_{CNT} + \mathbb{v}_{M} = 1 \tag{7}$$

In the end, the overall mechanical behavior of the nanocomposite construction is expressed as follows, according to Ref. [33].

$$\rho^{NCM} = \mathbb{v}_{CNT} \rho^{CNT} + \mathbb{v}_{M} \rho^{M} \tag{8a}$$

$$\nu^{NCM} = \nu^{M} \tag{8b}$$

$$\mathbb{G}^{NCM} = \frac{\mathbb{e}^{NCM}}{2(1 + \nu^{NCM})}. \tag{8c}$$

Additionally, the formula used to calculate the expansion parameters of the MHLN is taken from Ref. [34] as follows

$$\alpha_{11} = \frac{\mathbb{v}_f \mathbb{e}_{11}^f \alpha_{11}^f + \mathbb{v}_{NCM} \mathbb{e}^{NCM} \alpha^{NCM}}{\mathbb{v}_f \mathbb{e}_{11}^f + \mathbb{v}_{NCM} \mathbb{e}^{NCM}}, \tag{9a}$$

$$\alpha_{22} = (1 + \mathbb{v}_f)\mathbb{v}_f \alpha_{22}^f + (1 + \mathbb{v}_{NCM})\mathbb{v}_{NCM}\alpha_{NCM} - \nu_{12}\alpha_{11}, \tag{9b}$$

$$\alpha_{33} = \alpha_{22}. \tag{9c}$$

According to Ref. [35], the quantity α_{NCM} represents the coefficient of thermal expansion associated with the nanocomposite matrix

$$\alpha_{NCM} = \frac{1}{2}\{(\frac{\mathbb{v}_{CNT}\mathbb{e}_{11}^{CNT}\alpha_{11}^{CNT} + \mathbb{v}_m \mathbb{e}_m \alpha_m}{\mathbb{v}_{CNT}\mathbb{e}_{11}^{CNT} + \mathbb{v}_m \mathbb{e}_m})\}(1 - \nu^{NCM}) + (1 + \nu_m)\alpha_m \mathbb{v}_m + (1 + \nu^{CNT})\alpha^{CNT}\mathbb{v}_{CNT}. \tag{10}$$

3. Governing equations and associated boundary conditions:

According to the higher-order shear deformation theory (HSDT), the three translational movements along the coordinate axes are expressed through the following relations [36]:

$$\mathbb{u} = \mathbb{u}_0 + \mathbb{z}\mathbb{u}_1 + \mathbb{z}^2\mathbb{u}_2 + \mathbb{z}^3\mathbb{u}_3, \tag{11a}$$

$$\mathbb{v} = \mathbb{v}_0 + \mathbb{z}\mathbb{v}_1 + \mathbb{z}^2\mathbb{v}_2 + \mathbb{z}^3\mathbb{v}_3, \tag{11b}$$

$$\mathbb{w} = \mathbb{w}_0 + \mathbb{z}\mathbb{w}_1 + \mathbb{z}^2\mathbb{w}_2 + \mathbb{z}^3\mathbb{w}_3. \tag{11c}$$

The symbols $\mathbb{u}_0$, $\mathbb{v}_0$, and $\mathbb{w}_0$ denote the motion components along the radial, circumferential, and thickness axes, respectively. The angles of rotation of the mid-plane normal in the radial and circumferential directions are given by $\mathbb{u}_1$ and $\mathbb{v}_1$. The remaining variables—$\mathbb{u}_2$, $\mathbb{v}_2$, $\mathbb{u}_3$, $\mathbb{v}_3$, $\mathbb{w}_1$, $\mathbb{w}_2$, and $\mathbb{w}_3$—represent higher-order contributions from the Taylor series expansion, which capture more complex cross-sectional deformations across the thickness

3.1 Strains

The connection linking deformation to displacement is expressed in the following manner

$$\begin{aligned}
\mathfrak{E}_{\mathbb{rr}} &= \mathfrak{E}_{\mathbb{rr}}^{(0)} + \mathbb{z}\mathfrak{E}_{\mathbb{rr}}^{(1)} + \mathbb{z}^2\mathfrak{E}_{\mathbb{rr}}^{(2)} + \mathbb{z}^3\mathfrak{E}_{\mathbb{rr}}^{(3)},\\
\mathfrak{E}_{\theta\theta} &= \mathfrak{E}_{\theta\theta}^{(0)} + \mathbb{z}\mathfrak{E}_{\theta\theta}^{(1)} + \mathbb{z}^2\mathfrak{E}_{\theta\theta}^{(2)} + \mathbb{z}^3\mathfrak{E}_{\theta\theta}^{(3)},\\
\mathfrak{E}_{\mathbb{zz}} &= \mathfrak{E}_{\mathbb{zz}}^{(0)} + \mathbb{z}\mathfrak{E}_{\mathbb{zz}}^{(1)} + \mathbb{z}^2\mathfrak{E}_{\mathbb{zz}}^{(2)} + \mathbb{z}^3\mathfrak{E}_{\mathbb{zz}}^{(3)},\\
\mathfrak{E}_{\theta\mathbb{z}} &= \mathfrak{E}_{\theta\mathbb{z}}^{(0)} + \mathbb{z}\mathfrak{E}_{\theta\mathbb{z}}^{(1)} + \mathbb{z}^2\mathfrak{E}_{\theta\mathbb{z}}^{(2)} + \mathbb{z}^3\mathfrak{E}_{\theta\mathbb{z}}^{(3)},\\
\mathfrak{E}_{\mathbb{rz}} &= \mathfrak{E}_{\mathbb{rz}}^{(0)} + \mathbb{z}\mathfrak{E}_{\mathbb{rz}}^{(1)} + \mathbb{z}^2\mathfrak{E}_{\mathbb{rz}}^{(2)} + \mathbb{z}^3\mathfrak{E}_{\theta\mathbb{z}}^{(3)},\\
\mathfrak{E}_{\mathbb{r}\theta} &= \mathfrak{E}_{\mathbb{r}\theta}^{(0)} + \mathbb{z}\mathfrak{E}_{\mathbb{r}\theta}^{(1)} + \mathbb{z}^2\mathfrak{E}_{\mathbb{r}\theta}^{(2)} + \mathbb{z}^3\mathfrak{E}_{\mathbb{r}\theta}^{(3)}.
\end{aligned} \tag{12}$$

where:

$$\mathfrak{E}_{\mathbb{rr}}^{(0)}=\frac{\partial \mathbb{u}_0}{\partial \mathbb{r}},\ \mathfrak{E}_{\mathbb{rr}}^{(1)}=\frac{\partial \mathbb{u}_1}{\partial \mathbb{r}},\ \mathfrak{E}_{\mathbb{rr}}^{(2)}=\frac{\partial \mathbb{u}_2}{\partial \mathbb{r}},\ \mathfrak{E}_{\mathbb{rr}}^{(3)}=\frac{\partial \mathbb{u}_3}{\partial \mathbb{r}},$$

$$\mathfrak{E}_{\theta\theta}^{(0)}=\frac{1}{\mathbb{r}}\left(\mathbb{u}_0+\frac{\partial \mathbb{v}_0}{\partial \theta}\right),\ \mathfrak{E}_{\theta\theta}^{(1)}=\frac{1}{\mathbb{r}}\left(\mathbb{u}_1+\frac{\partial \mathbb{v}_1}{\partial \theta}\right),\ \mathfrak{E}_{\theta\theta}^{(2)}=\frac{1}{\mathbb{r}}\left(\mathbb{u}_2+\frac{\partial \mathbb{v}_2}{\partial \theta}\right),\ \mathfrak{E}_{\theta\theta}^{(3)}=\frac{1}{\mathbb{r}}\left(\mathbb{u}_3+\frac{\partial \mathbb{v}_3}{\partial \theta}\right),$$

$$\mathfrak{E}_{\mathbb{zz}}^{(0)}=\mathbb{w}_1,\ \mathfrak{E}_{\mathbb{zz}}^{(1)}=2\mathbb{w}_2,\ \mathfrak{E}_{\mathbb{zz}}^{(2)}=3\mathbb{w}_3,$$

$$\mathfrak{E}_{\mathbb{rz}}^{(0)}=\mathbb{u}_1+\frac{\partial \mathbb{w}_0}{\partial \mathbb{r}},\ \mathfrak{E}_{\mathbb{rz}}^{(1)}=2\mathbb{u}_2+\frac{\partial \mathbb{w}_1}{\partial \mathbb{r}},\ \mathfrak{E}_{\mathbb{rz}}^{(2)}=3\mathbb{u}_3+\frac{\partial \mathbb{w}_2}{\partial \mathbb{r}},\ \mathfrak{E}_{\mathbb{rz}}^{(3)}=\frac{\partial \mathbb{w}_3}{\partial \mathbb{r}}, \tag{13}$$

$$\mathfrak{E}_{\mathbb{r}\theta}^{(0)}=\frac{1}{\mathbb{r}}\left(\frac{\partial \mathbb{u}_0}{\partial \theta}-\mathbb{v}_0\right)+\frac{\partial \mathbb{v}_0}{\partial \mathbb{r}},\ \mathfrak{E}_{\mathbb{r}\theta}^{(1)}=\frac{1}{\mathbb{r}}\left(\frac{\partial \mathbb{u}_1}{\partial \theta}-\mathbb{v}_1\right)+\frac{\partial \mathbb{v}_1}{\partial \mathbb{r}},\ \mathfrak{E}_{\mathbb{r}\theta}^{(2)}=\frac{1}{\mathbb{r}}\left(\frac{\partial \mathbb{u}_2}{\partial \theta}-\mathbb{v}_2\right)+\frac{\partial \mathbb{v}_2}{\partial \mathbb{r}},$$

$$\mathfrak{E}_{\mathbb{r}\theta}^{(3)}=\frac{1}{\mathbb{r}}\left(\frac{\partial \mathbb{u}_3}{\partial \theta}-\mathbb{v}_3\right)+\frac{\partial \mathbb{v}_3}{\partial \mathbb{r}},$$

$$\mathfrak{E}_{\theta\mathbb{z}}^{(0)}=\mathbb{v}_1+\frac{1}{\mathbb{r}}\frac{\partial \mathbb{w}_0}{\partial \theta},\ \mathfrak{E}_{\theta\mathbb{z}}^{(1)}=2\mathbb{v}_2+\frac{1}{\mathbb{r}}\frac{\partial \mathbb{w}_1}{\partial \theta},\ \mathfrak{E}_{\theta\mathbb{z}}^{(2)}=3\mathbb{v}_3+\frac{1}{\mathbb{r}}\frac{\partial \mathbb{w}_2}{\partial \theta},\ \mathfrak{E}_{\theta\mathbb{z}}^{(3)}=\frac{1}{\mathbb{r}}\frac{\partial \mathbb{w}_3}{\partial \theta}.$$

3.2 Thermoelastic stress–strain relations

How the elastic stresses relate to strains is determined by the choice made about $\mathfrak{E}_{\mathbb{zz}}$. When $\mathfrak{E}_{\mathbb{zz}}$ is not zero—meaning the material can stretch through its thickness—the analysis relies on a three-dimensional formulation. For materials with functional gradation, the stress-strain relations take the form given below

$$\begin{Bmatrix}\mathcal{T}_{\mathbb{rr}}\\ \mathcal{T}_{\theta\theta}\\ \mathcal{T}_{\mathbb{zz}}\\ \mathcal{T}_{\theta\mathbb{z}}\\ \mathcal{T}_{\mathbb{rz}}\\ \mathcal{T}_{\mathbb{r}\theta}\end{Bmatrix}=\begin{bmatrix}\bar{\mathbb{q}}_{11} & \bar{\mathbb{q}}_{12} & \bar{\mathbb{q}}_{13} & 0 & 0 & 0\\ \bar{\mathbb{q}}_{12} & \bar{\mathbb{q}}_{22} & \bar{\mathbb{q}}_{23} & 0 & 0 & 0\\ \bar{\mathbb{q}}_{13} & \bar{\mathbb{q}}_{23} & \bar{\mathbb{q}}_{33} & 0 & 0 & 0\\ 0 & 0 & 0 & \bar{\mathbb{q}}_{44} & 0 & 0\\ 0 & 0 & 0 & 0 & \bar{\mathbb{q}}_{55} & 0\\ 0 & 0 & 0 & 0 & 0 & \bar{\mathbb{q}}_{66}\end{bmatrix}\begin{Bmatrix}\mathfrak{E}_{\mathbb{rr}}-\alpha_{11}\Delta T\\ \mathfrak{E}_{\theta\theta}-\alpha_{22}\Delta T\\ \mathfrak{E}_{\mathbb{zz}}-\alpha_{33}\Delta T\\ \mathfrak{E}_{\theta\mathbb{z}}\\ \mathfrak{E}_{\mathbb{rz}}\\ \mathfrak{E}_{\mathbb{r}\theta}\end{Bmatrix}, \tag{14}$$

where [37]

$$\bar{\mathbb{q}}_{11}=\mathbb{q}_{22}\,sin^4\Omega+2(\mathbb{q}_{12}+2\mathbb{q}_{66})\,sin^2\Omega\,cos^2\Omega+\mathbb{q}_{11}\,cos^4\Omega,$$

$$\bar{\mathbb{q}}_{12}=\mathbb{q}_{12}(cos^4\Omega+sin^4\Omega)+(\mathbb{q}_{22}+\mathbb{q}_{11}-4\mathbb{q}_{66})\,cos^2\Omega\,sin^2\Omega,$$

$$\bar{\mathbb{q}}_{13}=\mathbb{q}_{23}\,sin^2\Omega+\mathbb{q}_{13}\,cos^2\Omega,$$

$$\bar{\mathbb{q}}_{22}=\mathbb{q}_{11}\,sin^4\Omega+\mathbb{q}_{22}\,cos^4\Omega+2\mathbb{q}_{12}\,sin^2\Omega\,cos^2\Omega+2(\mathbb{q}_{12}+2\mathbb{q}_{66})\,cos^2\Omega\,sin^2\Omega, \tag{15}$$

$$\bar{\mathbb{q}}_{23}=\mathbb{q}_{23}\,cos^2\Omega+\mathbb{q}_{13}\,sin^2\Omega,$$

$$\bar{\mathbb{q}}_{33}=\mathbb{q}_{33},$$

$$\bar{\mathbb{q}}_{44}=\mathbb{q}_{55}\,sin^2\Omega+\mathbb{q}_{44}\,cos^2\Omega,$$

$$\bar{\mathbb{q}}_{55} = \mathbb{q}_{44}\, sin^2\, \Omega + \mathbb{q}_{55}\, cos^2\, \Omega,$$

$$\bar{\mathbb{q}}_{66} = \mathbb{q}_{66}(cos^2\, \Omega - sin^2\, \Omega)^2 - 4(2\mathbb{q}_{12} - \mathbb{q}_{11} - \mathbb{q}_{22})\, cos^2\, \Omega\, sin^2\, \Omega.$$

The Greek letter Ω indicates the orientation of the plies. Moreover, the quantities that appear in Eq. (15) are determined according to Ref. [49] in the following way.

$$\begin{gathered}
\mathbb{q}_{11} = \frac{(1-\nu_{32}\nu_{23})}{\Delta}\mathbb{e}_{11}\,, \quad \mathbb{q}_{12} = \frac{(\nu_{21}+\nu_{23}\nu_{31})}{\Delta}\mathbb{e}_{11}\,, \quad \mathbb{q}_{13} = \frac{(\nu_{31}+\nu_{32}\nu_{21})}{\Delta}\mathbb{e}_{11}, \\
\mathbb{q}_{22} = \frac{(1-\nu_{31}\nu_{13})}{\Delta}\mathbb{e}_{22}\,, \quad \mathbb{q}_{23} = \frac{(\nu_{32}+\nu_{31}\nu_{12})}{\Delta}\mathbb{e}_{22}\,, \quad \mathbb{q}_{33} = \frac{(1-\nu_{21}\nu_{12})}{\Delta}\mathbb{e}_{33}, \\
\mathbb{q}_{66} = \mathbb{G}_{12}, \mathbb{q}_{55} = \mathbb{G}_{23}, \mathbb{q}_{44} = \mathbb{G}_{13}, \\
\Delta = (1 - \nu_{32}\nu_{23} - \nu_{21}\nu_{12} - \nu_{31}\nu_{13} - 2\nu_{23}\nu_{31}\nu_{12}).
\end{gathered} \tag{16}$$

3.3 Governing equations and boundary conditions

Applying the principle of stationary total potential energy leads to the following expression [13]:

$$\delta(W - U) = 0 \tag{17}$$

By computing the first change in the elastic potential energy, the result is expressed as follows

$$\begin{gathered}
\delta U = \int_{\Omega_0} \left\{ \int_{-h/2}^{h/2} \left[\mathcal{T}_{\mathbb{rr}} \left(\delta\mathfrak{E}_{\mathbb{rr}}^{(0)} + \mathbb{z}\delta\mathfrak{E}_{\mathbb{rr}}^{(1)} + \mathbb{z}^2\delta\mathfrak{E}_{\mathbb{rr}}^{(2)} + \mathbb{z}^3\delta\mathfrak{E}_{\mathbb{rr}}^{(3)} \right) + \mathcal{T}_{\theta\theta} \left(\delta\mathfrak{E}_{\theta\theta}^{(0)} + \mathbb{z}\delta\mathfrak{E}_{\theta\theta}^{(1)} + \right.\right.\right. \\
\mathbb{z}^2\delta\mathfrak{E}_{\theta\theta}^{(2)} + \mathbb{z}^3\delta\mathfrak{E}_{\theta\theta}^{(3)} \Big) + \mathcal{T}_{\mathbb{r}\theta} \left(\delta\mathfrak{E}_{\mathbb{r}\theta}^{(0)} + \mathbb{z}\delta\mathfrak{E}_{\mathbb{r}\theta}^{(1)} + \mathbb{z}^2\delta\mathfrak{E}_{\mathbb{r}\theta}^{(2)} + \mathbb{z}^3\delta\mathfrak{E}_{\mathbb{r}\theta}^{(3)} \right) + \mathcal{T}_{\mathbb{rz}} \Big(\delta\mathfrak{E}_{\mathbb{rz}}^{(0)} + \mathbb{z}\delta\mathfrak{E}_{\mathbb{rz}}^{(1)} + \\
\mathbb{z}^2\delta\mathfrak{E}_{\mathbb{rz}}^{(2)} + \mathbb{z}^3\delta\mathfrak{E}_{\mathbb{rz}}^{(3)} \Big) + \mathcal{T}_{\theta\mathbb{z}} \left(\delta\mathfrak{E}_{\theta\mathbb{z}}^{(0)} + \mathbb{z}\delta\mathfrak{E}_{\theta\mathbb{z}}^{(1)} + \mathbb{z}^2\delta\mathfrak{E}_{\theta\mathbb{z}}^{(2)} + \mathbb{z}^3\delta\mathfrak{E}_{\theta\mathbb{z}}^{(3)} \right) + \mathcal{T}_{\mathbb{zz}} \Big(\delta\mathfrak{E}_{\mathbb{zz}}^{(0)} + \mathbb{z}\delta\mathfrak{E}_{\mathbb{zz}}^{(1)} + \\
\left.\left. \mathbb{z}^2\delta\mathfrak{E}_{\mathbb{zz}}^{(2)} + \mathbb{z}^3\delta\mathfrak{E}_{\mathbb{zz}}^{(3)} \Big) \right] d\mathbb{z} \right\} d\mathbb{r}d\theta.
\end{gathered} \tag{18}$$

Carrying out the depth-wise integration, the resulting expression for the elastic deformation energy is as follows

$$\begin{gathered}
\delta U = \int_{\Omega_0} \Big(\mathfrak{n}_{\mathbb{rr}}\delta\mathfrak{E}_{\mathbb{rr}}^{(0)} + \mathfrak{m}_{\mathbb{rr}}\delta\mathfrak{E}_{\mathbb{rr}}^{(1)} + \mathfrak{p}_{\mathbb{rr}}\delta\mathfrak{E}_{\mathbb{rr}}^{(2)} + \mathfrak{q}_{\mathbb{rr}}\delta\mathfrak{E}_{\mathbb{rr}}^{(3)} + \mathfrak{n}_{\theta\theta}\delta\mathfrak{E}_{\theta\theta}^{(0)} + \mathfrak{m}_{\theta\theta}\delta\mathfrak{E}_{\theta\theta}^{(1)} + \\
\mathfrak{p}_{\theta\theta}\delta\mathfrak{E}_{\theta\theta}^{(2)} + \mathfrak{q}_{\theta\theta}\delta\mathfrak{E}_{\theta\theta}^{(3)} + \mathfrak{n}_{\mathbb{r}\theta}\delta\mathfrak{E}_{\mathbb{r}\theta}^{(0)} + \mathfrak{m}_{\mathbb{r}\theta}\delta\mathfrak{E}_{\mathbb{r}\theta}^{(1)} + \mathfrak{p}_{\mathbb{r}\theta}\delta\mathfrak{E}_{\mathbb{r}\theta}^{(2)} + \mathfrak{q}_{\mathbb{r}\theta}\delta\mathfrak{E}_{\mathbb{r}\theta}^{(3)} + \mathfrak{n}_{\mathbb{rz}}\delta\mathfrak{E}_{\mathbb{rz}}^{(0)} + \\
\mathfrak{m}_{\mathbb{rz}}\delta\mathfrak{E}_{\mathbb{rz}}^{(1)} + \mathfrak{p}_{\mathbb{rz}}\delta\mathfrak{E}_{\mathbb{rz}}^{(2)} + \mathfrak{q}_{\mathbb{rz}}\delta\mathfrak{E}_{\mathbb{rz}}^{(3)} + \mathfrak{n}_{\theta\mathbb{z}}\delta\mathfrak{E}_{\theta\mathbb{z}}^{(0)} + \mathfrak{m}_{\theta\mathbb{z}}\delta\mathfrak{E}_{\theta\mathbb{z}}^{(1)} + \mathfrak{p}_{\theta\mathbb{z}}\delta\mathfrak{E}_{\theta\mathbb{z}}^{(2)} + \mathfrak{q}_{\theta\mathbb{z}}\delta\mathfrak{E}_{\theta\mathbb{z}}^{(3)} + \\
\mathfrak{n}_{\mathbb{zz}}\delta\mathfrak{E}_{\mathbb{zz}}^{(0)} + \mathfrak{m}_{\mathbb{zz}}\delta\mathfrak{E}_{\mathbb{zz}}^{(1)} + \mathfrak{p}_{\mathbb{zz}}\delta\mathfrak{E}_{\mathbb{zz}}^{(2)} + \mathfrak{q}_{\mathbb{zz}}\delta\mathfrak{E}_{\mathbb{zz}}^{(3)} \Big) d\mathbb{r}d\theta.
\end{gathered} \tag{19}$$

In this expression, Ω_0 refers to the two-dimensional region defined by the $\mathbb{r}$ and θ coordinates, and the corresponding force and moment quantities are obtained using the formula below

$$\left\{\mathfrak{n}_{ij}, \mathfrak{m}_{ij}, \mathfrak{p}_{ij}, \mathfrak{q}_{ij}\right\} = \int_{-h/2}^{h/2} \quad \{1, \mathbb{z}, \mathbb{z}^2, \mathbb{z}^3\}\mathcal{T}_{ij}d\mathbb{z}, \quad i = j = \mathbb{r}, \theta, \mathbb{z}. \tag{20a}$$

$$\left\{\mathfrak{n}_{ij}, \mathfrak{m}_{ij}, \mathfrak{p}_{ij}, \mathfrak{q}_{ij}\right\} = \int_{-h/2}^{h/2} \{1, \mathbb{z}, \mathbb{z}^2, \mathbb{z}^3\}\mathcal{T}_{ij} d\mathbb{z}, \quad i \neq j = \mathbb{r}, \theta, \mathbb{z}. \tag{20b}$$

Inside a cylindrical coordinate framework, the expression shown below describes a support structure made from auxetic material, known as a Haber-Schaim foundation [38]:

$$\delta W = \int_A \left(K_w \mathbb{w} + D_f \nabla^4 \mathbb{w}\right) \delta \mathbb{w} dA. \tag{21}$$

Let K_w, ν_f, and h_f stand for the Winkler stiffness, the lateral contraction ratio, and the thickness of the auxetic concrete base, respectively. Additionally, D_f is defined as $(\mathbb{e}_f {h_f}^3)$ / $[12(1-\nu_f^2)]$. Inserting the variations δU and δW into Eq. (17) yields the final motion equations and the edge conditions

4. Solution procedure

Solving the complicated differential equations derived earlier often requires numerical techniques, since closed-form answers exist only in very special cases. Therefore, we adopt the differential quadrature approach to estimate function derivatives. For a given function $\mathcal{f}$, its derivatives evaluated at a certain point can be written as shown below [39, 40]

$$\begin{aligned}
\left.\frac{\partial \mathcal{f}}{\partial \mathbb{r}}\right|_{\mathbb{r}=\mathbb{r}_{\mathbb{i}}, \theta=\theta_{\mathbb{j}}} &= \sum_{\mathbb{m}=1}^{\mathfrak{n}_{\mathbb{r}}} \sum_{\mathfrak{m}=1}^{\mathfrak{n}_\theta} \mathfrak{a}_{\mathbb{i}\mathbb{m}}^{\mathbb{z}}\, \mathfrak{i}_{\mathbb{j}\mathfrak{m}}^{\theta} \mathcal{f}_{\mathbb{m}\mathfrak{m}}, \\
\left.\frac{\partial \mathcal{f}}{\partial \theta}\right|_{\mathbb{r}=\mathbb{r}_{\mathbb{i}}, \theta=\theta_{\mathbb{j}}} &= \sum_{\mathbb{m}=1}^{\mathfrak{n}_{\mathbb{r}}} \sum_{\mathfrak{m}=1}^{\mathfrak{n}_\theta} \mathfrak{i}_{\mathbb{i}\mathbb{m}}^{\mathbb{r}}\, \mathfrak{a}_{\mathbb{j}\mathfrak{m}}^{\theta} \mathcal{f}_{\mathbb{m}\mathfrak{m}}, \\
\frac{\partial}{\partial \mathbb{r}}\left(\left.\frac{\partial \mathcal{f}}{\partial \theta}\right|_{\mathbb{r}=\mathbb{r}_{\mathbb{i}}, \theta=\theta_{\mathbb{j}}}\right) &= \sum_{\mathbb{m}=1}^{\mathfrak{n}_{\mathbb{r}}} \sum_{\mathfrak{m}=1}^{\mathfrak{n}_\theta} \mathfrak{a}_{\mathbb{i}\mathbb{m}}^{\mathbb{r}}\, \mathfrak{a}_{\mathbb{j}\mathfrak{m}}^{\theta} \mathcal{f}_{\mathbb{m}\mathfrak{m}}, \\
\left.\frac{\partial^2 \mathcal{f}}{\partial \mathbb{r}^2}\right|_{\mathbb{r}=\mathbb{r}_{\mathbb{i}}, \theta=\theta_{\mathbb{j}}} &= \sum_{\mathbb{m}=1}^{\mathfrak{n}_{\mathbb{r}}} \sum_{\mathfrak{m}=1}^{\mathfrak{n}_\theta} \mathfrak{b}_{\mathbb{i}\mathbb{m}}^{\mathbb{r}}\, \mathfrak{i}_{\mathbb{j}\mathfrak{m}}^{\theta} \mathcal{f}_{\mathbb{m}\mathfrak{m}}, \\
\left.\frac{\partial^2 \mathcal{f}}{\partial \theta^2}\right|_{\mathbb{r}=\mathbb{r}_{\mathbb{i}}, \theta=\theta_{\mathbb{j}}} &= \sum_{\mathbb{m}=1}^{\mathfrak{n}_{\mathbb{r}}} \sum_{\mathfrak{m}=1}^{\mathfrak{n}_\theta} \mathfrak{i}_{\mathbb{i}\mathbb{m}}^{\mathbb{r}}\, \mathfrak{b}_{\mathbb{j}\mathfrak{m}}^{\theta} \mathcal{f}_{\mathbb{m}\mathfrak{m}}.
\end{aligned} \tag{22}$$

Let the indices $\mathbb{i}$ and $\mathbb{m}$ each run from 1 to $\mathfrak{n}_{\mathbb{r}}$, while j and n each run from 1 to $\mathfrak{n}_\theta$. The quantity $\mathcal{f}_{\mathbb{m}\mathfrak{m}}$ denotes the function's value at the m-th point in the radial direction and the n-th point in the circumferential direction. The symbols $\mathfrak{i}_{\mathbb{i}\mathbb{m}}^{\mathbb{r}}$ and $\mathfrak{i}_{\mathbb{j}\mathfrak{m}}^{\theta}$ represent entries of the unit matrix. Finally, the weight coefficients $\mathfrak{a}_{\mathbb{i}\mathbb{m}}^{\mathbb{r}}$, $\mathfrak{a}_{\mathbb{j}\mathfrak{m}}^{\theta}$, $\mathfrak{b}_{\mathbb{i}\mathbb{m}}^{\mathbb{r}}$, and $\mathfrak{b}_{\mathbb{j}\mathfrak{m}}^{\theta}$ are given by the following expressions

$$\begin{aligned}
\mathfrak{a}_{\mathbb{i}\mathbb{m}}^{\mathbb{r}} &= \begin{cases} \dfrac{\lambda(\mathbb{r}_{\mathbb{i}})}{(\mathbb{r}_{\mathbb{i}}-\mathbb{r}_{\mathbb{m}})\lambda(\mathbb{r}_{\mathbb{m}})} & \mathbb{i} \neq \mathbb{m} \\ -\sum_{k=1, k\neq \mathbb{i}}^{\mathfrak{n}_{\mathbb{r}}} \mathfrak{a}_{\mathbb{i}k} & \mathbb{i} = \mathbb{m} \end{cases} \quad \mathbb{i}, \mathbb{m} = 1,2,\ldots,\mathfrak{n}_{\mathbb{r}}, \\
\mathfrak{a}_{\mathbb{j}\mathfrak{m}}^{\theta} &= \begin{cases} \dfrac{\hbar(\theta_{\mathbb{j}})}{(\theta_{\mathbb{j}}-\theta_{\mathfrak{m}})\lambda(\theta_{\mathfrak{m}})} & \mathbb{j} \neq \mathfrak{m} \\ -\sum_{k=1, k\neq \mathbb{j}}^{\mathfrak{n}_\theta} \mathfrak{a}_{\mathbb{j}k} & \mathbb{j} = \mathfrak{m} \end{cases} \quad \mathbb{j}, \mathfrak{m} = 1,2,\ldots,\mathfrak{n}_\theta.
\end{aligned} \tag{23}$$

in the above equations,

$$
\begin{aligned}
\lambda(\mathbb{r}_{\mathbb{i}}) &= \prod_{k=1,k\neq \mathbb{i}}^{\mathbb{n}_{\mathbb{r}}}(\mathbb{r}_{\mathbb{i}}-\mathbb{r}_k),\\
\lambda(\mathbb{r}_{\mathbb{m}\mathbb{m}}) &= \prod_{k\neq \mathbb{m}\mathbb{m},k=1}^{\mathbb{n}_{\mathbb{r}}}(\mathbb{r}_{\mathbb{m}\mathbb{m}}-\mathbb{r}_k),\\
\hbar(\theta_{\mathbb{j}}) &= \prod_{k=1,k\neq \mathbb{j}}^{\mathbb{n}_{\theta}}(\theta_{\mathbb{j}}-\theta_k),\\
\hbar(\theta_{\mathbb{m}}) &= \prod_{k\neq \mathbb{m},k=1}^{\mathbb{n}_{\theta}}(\theta_{\mathbb{m}}-\theta_k).
\end{aligned}
\tag{24}
$$

and

$$
\begin{aligned}
\mathbb{b}_{\mathbb{i}\mathbb{m}\mathbb{m}}^{\mathbb{r}} &= 2\left(\mathbb{a}_{\mathbb{i}\mathbb{i}}^{\mathbb{r}}\mathbb{a}_{\mathbb{i}\mathbb{m}\mathbb{m}}^{\mathbb{r}}-\frac{\mathbb{a}_{\mathbb{i}\mathbb{m}\mathbb{m}}^{\mathbb{r}}}{(\mathbb{r}_{\mathbb{i}}-\mathbb{r}_{\mathbb{m}\mathbb{m}})}\right),\ \mathbb{i},\mathbb{m}\mathbb{m}=1,2,\ldots,\mathbb{n}_{\mathbb{r}},\mathbb{i}\neq \mathbb{m}\mathbb{m}\\
\mathbb{b}_{\mathbb{j}\mathbb{m}}^{\theta} &= 2\left(\mathbb{a}_{\mathbb{j}\mathbb{j}}^{\theta}\mathbb{a}_{\mathbb{j}\mathbb{m}}^{\theta}-\frac{\mathbb{a}_{\mathbb{j}\mathbb{m}}^{\theta}}{(\theta_{\mathbb{j}}-\theta_{\mathbb{m}})}\right),\ \mathbb{j},\mathbb{m}=1,2,\ldots,\mathbb{n}_{\theta},\mathbb{j}\neq \mathbb{m}\\
\mathbb{b}_{\mathbb{i}\mathbb{i}}^{\mathbb{r}} &= -\sum_{k=1,k\neq \mathbb{i}}^{\mathbb{n}_{\mathbb{r}}}\mathbb{b}_{\mathbb{i}k}^{\mathbb{r}},\ \mathbb{i}=1,2,\ldots,\mathbb{n}_{\mathbb{r}}\quad \mathbb{i}=\mathbb{m}\mathbb{m}\\
\mathbb{b}_{\mathbb{j}\mathbb{j}}^{\theta} &= -\sum_{k=1,k\neq \mathbb{j}}^{\mathbb{n}_{\theta}}\mathbb{b}_{\mathbb{j}k}^{\theta},\quad \mathbb{j}=1,2,\ldots,\mathbb{n}_{\theta}\quad \mathbb{j}=\mathbb{m}
\end{aligned}
\tag{25}
$$

Furthermore, a Chebyshev-Gauss-Lobatto grid layout [41] is adopted, where the positions of the nodal points, denoted by $(\mathbb{r}_{\mathbb{i}},\theta_{\mathbb{j}})$, on the reference surface are given as follows [41]:

$$
\begin{aligned}
\mathbb{r}_{\mathbb{i}} &= R_i+\frac{R_o-R_i}{2}\left(1-cos\left(\frac{(\mathbb{i}-1)}{(\mathbb{n}_{\mathbb{r}}-1)}\pi\right)\right),\quad \mathbb{i}=1,2,3,\ldots,\mathbb{n}_{\mathbb{r}}\\
\theta_{\mathbb{j}} &= \frac{\theta_m}{2}\left(1-cos\left(\frac{(\mathbb{j}-1)}{(\mathbb{n}_{\theta}-1)}\pi\right)\right),\quad \mathbb{j}=1,2,3,\ldots,\mathbb{n}_{\theta}
\end{aligned}
\tag{26}
$$

As a result, the eigenvalue problem in algebraic form can be expressed using matrix notation as follows:

$$(\mathrm{K_L}-\Delta T\mathrm{K_T})\mathrm{d}=0. \tag{27}$$

The quantities in both $\mathrm{K_L}$ and $\mathrm{K_T}$ remain fixed. By dropping the nonlinear matrices, Eq. (27) reduces to a standard linear eigenvalue form. The smallest positive eigenvalue, denoted $\Delta\mathrm{T}_{cr}$, corresponds to the critical temperature rise that triggers buckling in an annular plate. A four-character code defines the edge restrictions: the first character indicates the condition at the inner radius $\mathbb{r}=R_{\mathbb{i}}$, the second at $\theta = 0$, the third at the outer radius $\mathbb{r}=R_o$, and the fourth at $\theta=\theta_m$. Next, a parametric study is carried out to assess how various parameters affect the buckling behavior of the MHL annular sector plate. Refs. [42, 43] provide the geometric and physical data for the constituent materials.

5. Results and discussion

5.1 Verification

Table 1 has presented a comparative validation study for the critical thermal buckling temperature difference ΔT_{cr} [K] of functionally graded graphene platelet reinforced composite (FG-GPLRC)

Table 1. A comparison study between the Critical buckling temperature difference ΔT_{cr} [K] of the FG-GPLRC sector plates with $R_o/R_i = 1/5$, $R_i/h = 40$, $W_{GPL} = 0.3\%$, $\theta_m = 60°$, and GPL-UD

	Ref. [44]	Present
SSSS	29.3956	29.3833
CCCC	96.7456	96.7394

annular sector plates. The comparison has been peFrformed between the reference solution reported in Ref. [44] and the present computational formulation. The analysis has considered the geometric and material parameters $R_o/R_i = 1/5$, $R_i/h = 40$, $W_{GPL} = 0.3\%$, $\theta_m = 60°$, under the GPL-UD distribution pattern. Two classical boundary conditions have been examined, namely simply supported on all edges (SSSS) and fully clamped on all edges (CCCC). For the SSSS boundary condition, the reference value of the critical buckling temperature difference has been reported as 29.3956 K, whereas the present model has predicted 29.3833 K. Similarly, for the CCCC boundary condition, the reference and present results have been obtained as 96.7456 K and 96.7394 K, respectively. The extremely small discrepancies between the two sets of results have demonstrated the excellent accuracy, numerical stability, and convergence capability of the present formulation. Therefore, the comparison has verified that the adopted higher-order mathematical modeling, combined with the differential quadrature method, has provided reliable predictions for the thermal buckling behavior of hybrid nanocomposite annular plates supported by auxetic elastic foundations.

5.2 Parametric results

Fig. 2 has illustrated the influence of the annular sector angle on the critical thermal buckling temperature difference ΔT_{cr} $[K]$ for hybrid nanocomposite annular plates subjected to different boundary conditions. The graph has compared the thermal stability responses of simply supported and fully clamped plates over a sector angle range from 20° to 90°. The results have demonstrated that the critical buckling temperature has decreased significantly as the annular angle increased. This behavior has indicated that larger sector openings reduced the structural stiffness and consequently weakened the thermal stability resistance of the annular plate. For the SSSS boundary condition, the critical temperature difference has gradually declined from approximately 45° at $\theta_m = 20^{\circ}$ to nearly 37° at $\theta_m = 90^{\circ}$. In contrast, the CCCC boundary condition has exhibited substantially higher thermal resistance throughout the entire angular range, decreasing from about 93° to nearly 42°. The clamped configuration has therefore provided stronger edge constraints, resulting in improved resistance against thermally induced instability. Moreover, the figure has revealed that the rate of reduction in ΔT_{cr} became less pronounced at larger sector angles, suggesting a gradual stabilization trend. These findings have confirmed that both geometric configuration and boundary conditions have played essential roles in the management and optimization of thermal buckling performance in annular nanocomposite plate structures.

Fig. 3 has demonstrated the influence of laminated layer configuration on the critical thermal buckling temperature difference of hybrid nanocomposite annular plates subjected to varying annular sector angles θ_m. Three different symmetric laminate stacking sequences have been investigated, namely $[90°, 0°, 90°]$, $[90°, 0°, 90°, 0°, 90°]$, and $[90°, 0°, 90°, 0°, 90°, 0°, 90°]$. The obtained results have revealed that both the number of laminated layers and fiber orientation arrangements have significantly affected the thermal stability behavior of the structure. The figure

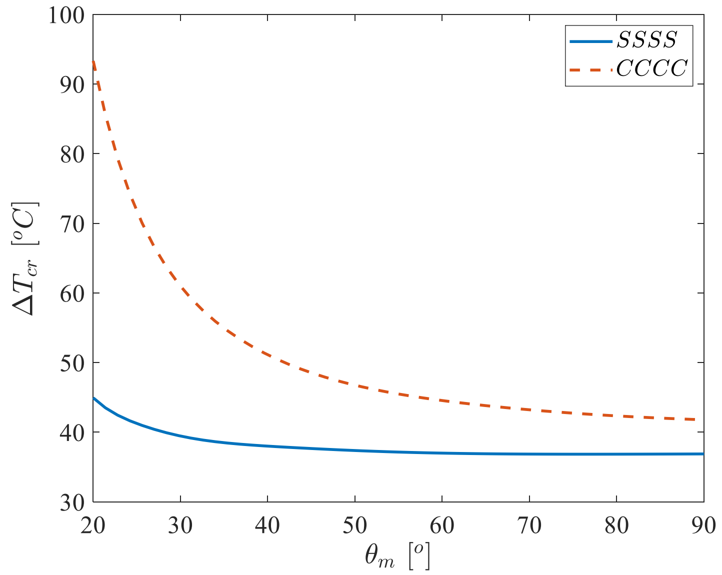

Figure 2. The influence of the annular sector angle on the critical thermal buckling temperature difference for hybrid nanocomposite annular plates for different boundary conditions

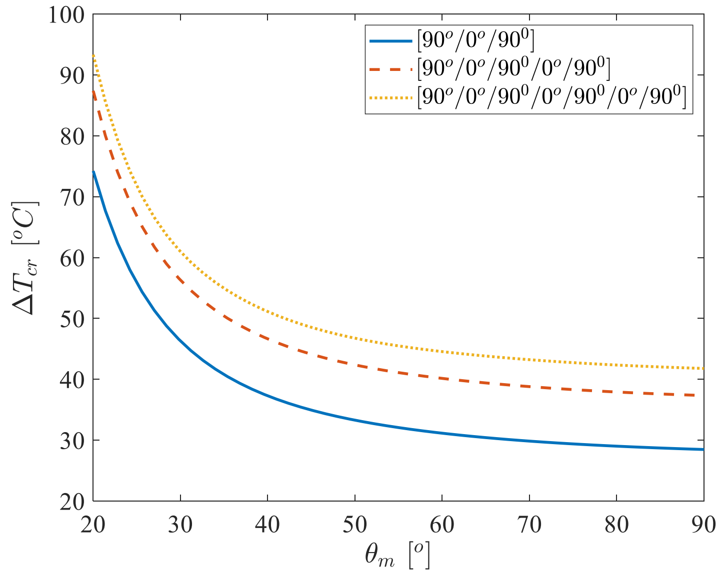

Figure 3. The influence of laminated layer configuration on the critical thermal buckling temperature difference of hybrid nanocomposite annular plates subjected to varying annular sector angles and symmetric laminate stacking sequences

has shown that the critical buckling temperature difference decreased continuously as the annular sector angle increased from 20° to 90°. This reduction has indicated that larger sector openings weakened the structural rigidity and reduced resistance against thermally induced instability. However, increasing the number of laminate layers has consistently enhanced the thermal buckling

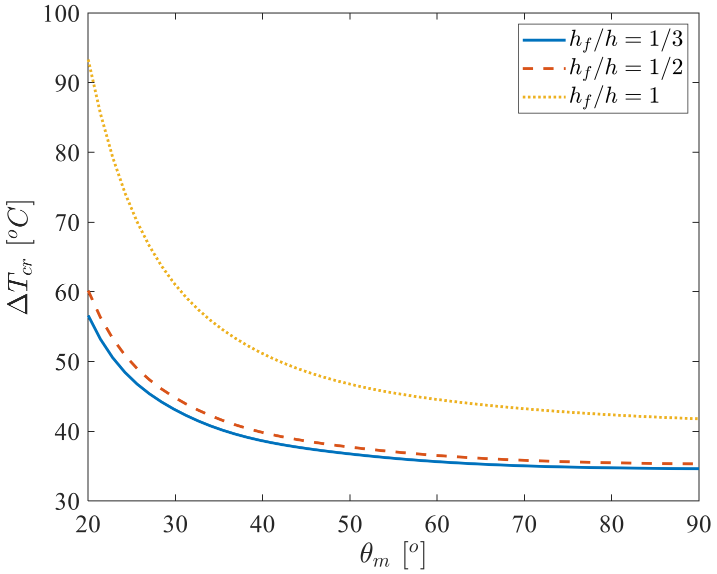

Figure 4. The effect of the auxetic elastic foundation thickness ratio on the critical thermal buckling temperature difference of hybrid nanocomposite annular plates

resistance. The seven-layer laminate configuration has produced the highest ΔT_{cr} values across the entire angular range, while the three-layer laminate has exhibited the lowest thermal stability performance. Furthermore, the results have demonstrated that multilayer symmetric laminations improved bending stiffness and stress redistribution within the annular plate. The difference between laminate configurations became more noticeable at smaller sector angles, where structural stiffness effects were more dominant. Consequently, the figure has confirmed that optimized laminated stacking sequences have played a crucial role in the management and enhancement of thermal buckling resistance in advanced hybrid nanocomposite annular plate systems supported by auxetic elastic foundations.

Fig. 4 illustrates the effect of the auxetic elastic foundation thickness ratio on the critical thermal buckling temperature difference ΔT_{cr} of hybrid nanocomposite annular plates. Three different foundation thickness ratios, namely h_f/h=1/3, 1/2, and 1, have been considered to evaluate the influence of the auxetic substrate on thermal stability performance over varying annular sector angles. The results have demonstrated that increasing the auxetic foundation thickness significantly enhanced the thermal buckling resistance of the annular plate structure. The figure has shown that all configurations experienced a gradual reduction in the critical buckling temperature difference as the sector angle increased from 20° to 90°. This trend has indicated that larger annular openings reduced the global stiffness and weakened the structural resistance against thermally induced instability. However, thicker auxetic foundations consistently produced higher ΔT_{cr} values throughout the entire angular range. In particular, the configuration with h_f/h=1 has exhibited the highest thermal stability, while the case with h_f/h =1/3 has shown the lowest resistance to thermal buckling. Furthermore, the influence of foundation thickness has been more pronounced at smaller sector angles, where the interaction between the plate and the auxetic substrate became stronger. The enhanced stiffness contribution provided by the thicker auxetic

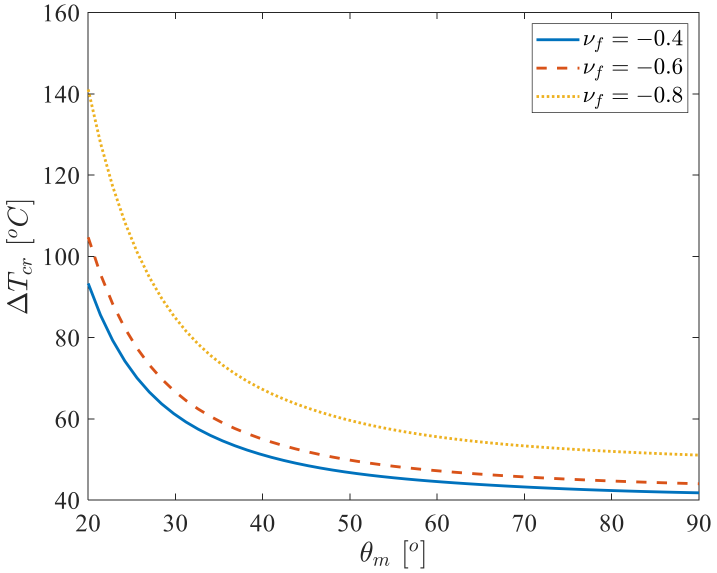

Figure 5. The influence of the auxetic foundation Poisson's ratio parameter on the critical thermal buckling temperature difference of hybrid nanocomposite annular plates

foundation has improved load distribution and reduced deformation sensitivity under thermal loading conditions. Consequently, the results have confirmed that the thickness of the auxetic elastic foundation has played a critical role in the management and optimization of thermal stability behavior in advanced laminated nanocomposite annular plate systems.

Fig. 5 presents the influence of the auxetic foundation Poisson's ratio parameter on the critical thermal buckling temperature difference ΔT_{cr} of hybrid nanocomposite annular plates. Three negative Poisson's ratio values, namely $\nu_f = -0.4, -0.6,$ and -0.8, have been investigated to evaluate the contribution of auxetic behavior to thermal stability enhancement. The results have clearly demonstrated that stronger auxetic characteristics, corresponding to more negative Poisson's ratio values, significantly improved the resistance of the annular plate against thermal buckling. The figure has shown that the critical buckling temperature difference decreased continuously as the annular sector angle increased from 20° to 90°. This reduction has indicated that larger sector openings weakened the structural stiffness and increased susceptibility to thermally induced instability. Nevertheless, the configuration with $\nu_f = -0.8$ has consistently exhibited the highest ΔT_{cr} values throughout the entire angular range, while the case with $\nu_f = -0.4$ has produced the lowest thermal stability performance. Furthermore, the enhancement provided by the auxetic foundation has been particularly significant at smaller sector angles, where the plate–foundation interaction became more dominant. The negative Poisson's ratio effect has increased the effective stiffness and improved stress redistribution under thermal loading conditions. Consequently, the results have confirmed that the auxetic Poisson's ratio parameter has played a crucial role in the management, optimization, and stabilization of advanced nanocomposite annular plate systems subjected to severe thermo-mechanical environments.

Fig. 6 has illustrated the effect of the Winkler foundation coefficient on the critical thermal buckling temperature difference ΔT_{cr} of hybrid nanocomposite annular plates subjected to varying

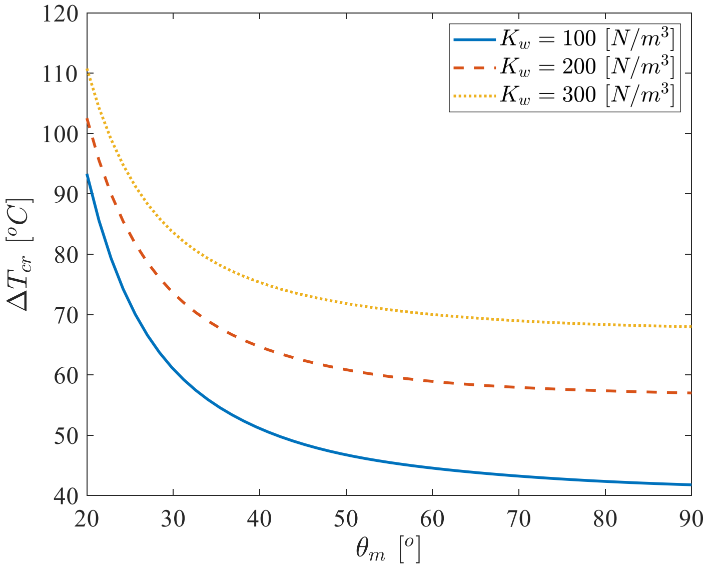

Figure 6. The effect of the Winkler foundation coefficient on the critical thermal buckling temperature difference of hybrid nanocomposite annular plates

annular sector angles. Three different Winkler stiffness parameters, namely $K_w = 100[N/m^3]$, $200[N/m^3]$, and $300[N/m^3]$, have been considered to evaluate the role of elastic foundation stiffness in enhancing thermo-mechanical stability. The results have demonstrated that increasing the Winkler coefficient significantly improved the thermal buckling resistance of the annular plate system. The figure has shown that the critical buckling temperature difference decreased progressively as the annular sector angle increased from 20° to 90°. This behavior has indicated that larger sector openings reduced the global structural stiffness and weakened resistance against thermal instability. Nevertheless, higher Winkler foundation stiffness values consistently produced greater ΔT_{cr} values throughout the entire angular range. In particular, the case with $K_w = 300[N/m^3]$ has exhibited the highest thermal stability performance, while the configuration with $K_w = 100[N/m^3]$ has shown the lowest resistance to thermal buckling. Furthermore, the influence of the Winkler coefficient has been more pronounced at smaller annular sector angles, where the interaction between the nanocomposite plate and the elastic substrate became stronger. The increased foundation stiffness has enhanced load-carrying capacity, improved stress redistribution, and reduced transverse deformation under thermal loading conditions. Consequently, the results have confirmed that the Winkler foundation parameter has played a significant role in the management and optimization of thermal buckling stability in advanced hybrid laminated nanocomposite annular plate structures supported by auxetic elastic foundations.

Fig. 7 shows the influence of the geometric radius ratio on the critical thermal buckling temperature difference ΔT_{cr} of hybrid nanocomposite annular plates subjected to varying annular sector angles. Three radius ratios, namely R_o/R_i=3, 4, and 5, have been examined to evaluate the effect of annular geometry on thermo-mechanical stability behavior. The results have revealed that the radius ratio has played a significant role in determining the structural stiffness and thermal buckling resistance of the annular plate system. The figure has shown that the critical buckling temperature difference decreased continuously with increasing annular sector angle from 20° to

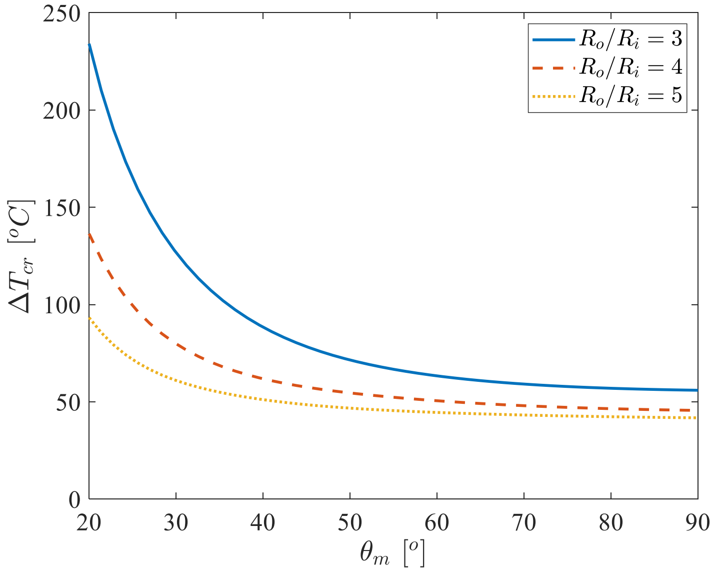

Figure 7. the influence of the geometric radius ratio on the critical thermal buckling temperature difference ΔT_{cr} of hybrid nanocomposite annular plates subjected to varying annular sector angles

90°. This trend has indicated that larger sector openings weakened the structural rigidity and reduced the resistance against thermally induced instability. In addition, increasing the radius ratio from 3 to 5 has caused a noticeable reduction in ΔT_{cr}. The configuration with R_o/R_i=3 has exhibited the highest thermal stability performance, whereas the case with R_o/R_i=5 has shown the lowest critical buckling resistance. Furthermore, the influence of the radius ratio has been more significant at smaller annular sector angles, where geometric stiffness effects became dominant. Larger radius ratios increased the flexibility of the annular plate and reduced its ability to sustain thermal loading without instability. Consequently, the results have confirmed that the annular geometric ratio has represented a crucial design parameter in the management and optimization of thermal buckling behavior in advanced hybrid laminated nanocomposite plate structures supported by auxetic elastic foundations.

Fig. 8 shows the influence of the carbon nanotube weight fraction on the critical thermal buckling temperature difference ΔT_{cr} of hybrid laminated nanocomposite annular plates subjected to varying annular sector angles. Three CNT reinforcement contents, namely $W_{cnt} = 0.1, 0.2,$ and 0.3 $[wt\%]$, have been investigated to evaluate the contribution of nanofiller concentration to thermo-mechanical stability enhancement. The obtained results have demonstrated that increasing the CNT weight fraction significantly improved the thermal buckling resistance of the annular plate structure. The figure has shown that the critical buckling temperature difference decreased continuously as the annular sector angle increased from 20° to 90°. This reduction has indicated that larger annular openings weakened the structural stiffness and increased susceptibility to thermally induced instability. However, higher CNT reinforcement levels consistently produced larger ΔT_{cr} values throughout the entire angular range. In particular, the configuration with $W_{cnt} = 0.3$ $[wt\%]$ has exhibited the highest thermal stability performance, whereas the case with $W_{cnt} = 0.1$ $[wt\%]$ has shown the lowest resistance against thermal buckling. Furthermore, the strengthening effect of CNT reinforcement has been more pronounced at smaller sector angles,

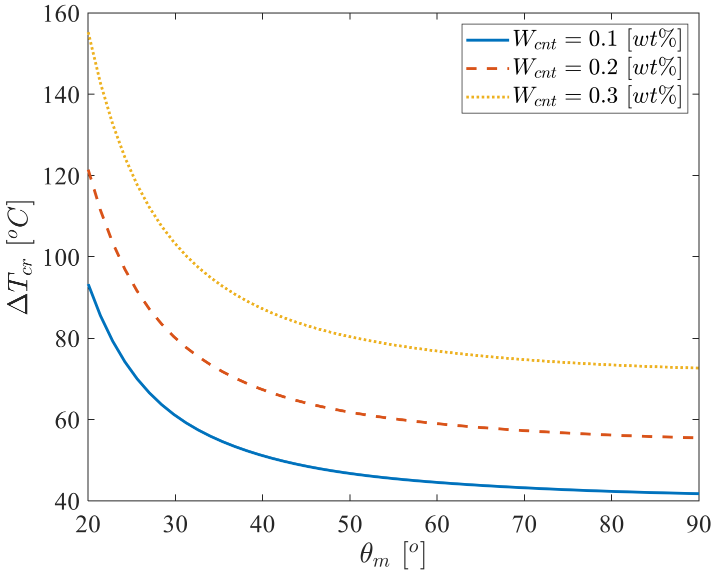

Figure 8. The influence of the carbon nanotube weight fraction on the critical thermal buckling temperature difference of hybrid laminated nanocomposite annular plates subjected to varying annular sector angles

where stiffness enhancement dominated the structural response. The incorporation of higher CNT content has improved elastic rigidity, stress transfer capability, and thermal resistance within the laminated nanocomposite layers. Consequently, the results have confirmed that the CNT weight fraction has represented a critical material design parameter in the management and optimization of thermal buckling stability for advanced annular nanocomposite plate systems supported by auxetic elastic foundations.

6. Conclusions

In conclusion, the present study has provided a comprehensive investigation into the thermal buckling management and stability enhancement of hybrid nanocomposite reinforced annular plates resting on an auxetic elastic foundation. The developed multi-scale hybrid laminated nanocomposite formulation has successfully captured the complex interaction between nano-reinforcement characteristics and thermo-mechanical loading conditions. By employing higher-order shear deformation theory, the analysis has accurately represented transverse shear deformation effects and thickness-dependent responses that have frequently been neglected in classical plate formulations. Moreover, thermoelastic stress–strain relations have effectively described the coupling between temperature variation and structural deformation behavior under critical thermal environments. The Haber–Schaim auxetic elastic foundation model has demonstrated a significant contribution to stiffness enhancement and stability improvement due to the negative Poisson’s ratio characteristics of the surrounding substrate. The obtained numerical findings have indicated that the auxetic foundation parameters, nanoparticle volume fraction, geometric configuration, and lamination sequence have substantially influenced the critical thermal buckling temperature and post-buckling resistance of the annular plates. Furthermore, the differential quadrature method based on Chebyshev–Gauss–Lobatto grid points has achieved high numerical accuracy, rapid convergence, and computational efficiency in solving the governing equations. The parametric investigations have revealed that optimized hybrid nanocomposite distributions and properly selected auxetic foundation coefficients have considerably enhanced structural reliability and thermal resistance. Consequently, the proposed framework has established an efficient management strategy for the design and control of advanced nanocomposite structural systems subjected to severe thermal conditions. The outcomes of this research have contributed valuable theoretical and practical insights for future aerospace, mechanical, marine, and energy engineering applications where lightweight, thermally stable, and high-performance composite structures have become increasingly essential.

Acknowledgment

The authors extend their appreciation to the Deanship of Scientific Research at Northern Border University, Arar, KSA for funding this research work through the project number "NBU-FFR-2026-1161-XX''.

References

1. Abderezak, R., Rabia, B., Daouadji, T.H., Abbes, B., Belkacem, A., Abbes, F. (2018). Elastic analysis of interfacial stresses in prestressed PFGM-RC hybrid beams. Advances in Materials Research, 7(2), 83-98. https://doi.org/10.12989/amr.2018.7.2.083
2. Akinnawo, S.O. (2024). Advance nanocomposites from biopolymers and fillers: Sources, characterization, and end-use applications. Polymer-Plastics Technology and Materials, 63(5), 570-604. https://doi.org/10.1080/25740881.2023.2284837
3. Al-Bahrani, M., Bouaissi, A., Cree, A. (2021). Mechanical and electrical behaviors of self-sensing nanocomposite-based MWCNTs material when subjected to twist shear load. Mechanics of Advanced Materials and Structures, 28(14), 1488-1497. https://doi.org/10.1080/15376494.2019.1672220
4. Al-Furjan, M., Fan, S., Shan, L., Farrokhian, A., Shen, X., Kolahchi, R. (2023). Wave propagation analysis of micro air vehicle wings with honeycomb core covered by porous FGM and nanocomposite magnetostrictive layers. Waves in Random and Complex Media, 33(4), 1-30. https://doi.org/10.1080/17455030.2021.1965211
5. Ali, A.Y., Hasan, H.M., Mohammed, F.M. (2024). Nonlinear dynamic buckling of a simply supported imperfect nanocomposite shear deformable plate under the effect of in-plane velocities. Communications in Nonlinear Science and Numerical Simulation, 138, Article 108232. https://doi.org/10.1016/j.cnsns.2024.108232
6. Amari, A., Hassan, Z.K., Al-Bahrani, M., Saberi, L., Maktoof, M.A.J. (2024). Practical parameter tuning toward enhancing thermomechanical shock resistance of the nanocomposite structure. Mechanics of Advanced Materials and Structures, 31(9), 1897-1916. https://doi.org/10.1080/15376494.2022.2135780
7. Aminipour, H., Janghorban, M., Li, L. (2018). A new model for wave propagation in functionally graded anisotropic doubly-curved shells. Composite Structures, 190, 91-111. https://doi.org/10.1016/j.compstruct.2018.02.028
8. Arshid, E., Amir, S., Loghman, A. (2020). Static and dynamic analyses of FG-GNPs reinforced porous nanocomposite annular micro-plates based on MSGT. International Journal of Mechanical Sciences, 180, Article 105656. https://doi.org/10.1016/j.ijmecsci.2020.105656
9. Avey, M., Fantuzzi, N., Sofiyev, A. (2023). Thermoelastic stability of CNT patterned conical shells

under thermal loading in the framework of shear deformation theory. Mechanics of Advanced Materials and Structures, 30(9), 1828-1841. https://doi.org/10.1080/15376494.2022.2054308
10. Babaei, H., Zavari, S., Kaveh, A., Arshid, E., Civalek, Ö. (2024). Dynamic response of advanced lightweight porous plates integrated with nanocomposite face sheets resting on elastic substrate. International Journal of Structural Stability and Dynamics, 24(12), Article 2550132. https://doi.org/10.1142/S021945542550132X
11. Bagheri, H., Kiani, Y., Eslami, M. (2017). Asymmetric thermo-inertial buckling of annular plates. Acta Mechanica, 228(4), 1493-1509. https://doi.org/10.1007/s00707-016-1789-z
12. Bakhtiari, M., Tarkashvand, A., Daneshjou, K. (2020). Plane-strain wave propagation of an impulse-excited fluid-filled functionally graded cylinder containing an internally clamped shell. Thin-Walled Structures, 149, Article 106482. https://doi.org/10.1016/j.tws.2019.106482
13. Caliskan, U., Gulsen, H., Apalak, M.K. (2024). New approach for modeling randomly distributed CNT reinforced polymer nanocomposite with van der Waals interactions. Mechanics of Advanced Materials and Structures, 31(1), 218-229. https://doi.org/10.1080/15376494.2022.2158963
14. Chen, D., Yang, J., Kitipornchai, S. (2017). Nonlinear vibration and postbuckling of functionally graded graphene reinforced porous nanocomposite beams. Composites Science and Technology, 142, 235-245. https://doi.org/10.1016/j.compscitech.2017.02.008
15. Cong, P.H., Trung, V.D., Khoa, N.D., Duc, N.D. (2022). Vibration and nonlinear dynamic response of temperature-dependent FG-CNTRC laminated double curved shallow shell with positive and negative Poisson's ratio. Thin-Walled Structures, 171, Article 108713. https://doi.org/10.1016/j.tws.2021.108713
16. Ebrahimi, F., Dabbagh, A. (2019a). On thermo-mechanical vibration analysis of multi-scale hybrid composite beams. Journal of Vibration and Control, 25(4), 933-945. https://doi.org/10.1177/1077546318806800
17. Ebrahimi, F., Dabbagh, A. (2019b). Vibration analysis of multi-scale hybrid nanocomposite plates based on a Halpin-Tsai homogenization model. Composites Part B: Engineering, 173, Article 106955. https://doi.org/10.1016/j.compositesb.2019.106955
18. Ebrahimi, F., Habibi, S. (2018). Nonlinear eccentric low-velocity impact response of a polymer-carbon nanotube-fiber multiscale nanocomposite plate resting on elastic foundations in hygrothermal environments. Mechanics of Advanced Materials and Structures, 25(5), 425-438. https://doi.org/10.1080/15376494.2017.1285453
19. El Jery, A., Al-Bahrani, M., Alatba, S.R., Fraga, M. (2024). Simultaneous effect of thermal shock and prebuckling loads on the exact coupled thermoelasticity response of the nanocomposite-reinforced sandwich sector system. Mechanics of Advanced Materials and Structures, 31(12), 2648-2666. https://doi.org/10.1080/15376494.2023.2184315
20. Eringen, A.C., Wegner, J. (2003). Nonlocal continuum field theories. Applied Mechanics Reviews, 56(2), B20-B22. https://doi.org/10.1115/1.1553434
21. Gao, W., Qin, Z., Chu, F. (2020). Wave propagation in functionally graded porous plates reinforced with graphene platelets. Aerospace Science and Technology, 102, Article 105860. https://doi.org/10.1016/j.ast.2020.105860
22. Garg, A., Belarbi, M.O., Li, L., Chalak, H.D., Tounsi, A., Zenkour, A.M. (2024). Comparative study on the buckling analysis of exponential, power and sigmoidal sandwich FGM plates under hygro-thermal conditions. Advances in Materials Research, 13(4), 431-462. https://doi.org/10.12989/amr.2024.13.6.431
23. Jha, D., Kant, T., Singh, R.K. (2012). Higher order shear and normal deformation theory for natural frequency of functionally graded rectangular plates. Nuclear Engineering and Design, 250, 8-13. https://doi.org/10.1016/j.nucengdes.2012.05.037
24. Javani, M., Kiani, Y., Eslami, M. (2020). Thermal buckling of FG graphene platelet reinforced composite annular sector plates. Thin-Walled Structures, 148, Article 106589. https://doi.org/10.1016/j.tws.2019.106589
25. Karami, B., Shahsavari, D., Janghorban, M. (2018). Wave propagation analysis in functionally graded (FG) nanoplates under in-plane magnetic field based on nonlocal strain gradient theory and four

variable refined plate theory. Mechanics of Advanced Materials and Structures, 25(12), 1047-1057. https://doi.org/10.1080/15376494.2017.1329468
26. Karimiasl, M., Ebrahimi, F., Akgöz, B. (2019). Buckling and post-buckling responses of smart doubly curved composite shallow shells embedded in SMA fiber under hygro-thermal loading. Composite Structures, 223, Article 110988. https://doi.org/10.1016/j.compstruct.2019.110988
27. Kim, M., Park, Y.B., Okoli, O.I., Zhang, C. (2009). Processing, characterization, and modeling of carbon nanotube-reinforced multiscale composites. Composites Science and Technology, 69(3-4), 335-342. https://doi.org/10.1016/j.compscitech.2008.10.019
28. Kumar, S. (2023). Parametric study of CNT waviness effect in CNT/polymer nanocomposites using multiscale finite element modeling. Mechanics of Advanced Materials and Structures, 30(25), 1-11. https://doi.org/10.1080/15376494.2022.2134037
29. Lim, C., Zhang, G., Reddy, J. (2015). A higher-order nonlocal elasticity and strain gradient theory and its applications in wave propagation. Journal of the Mechanics and Physics of Solids, 78, 298-313. https://doi.org/10.1016/j.jmps.2015.02.008
30. Nebab, M., Atmane, H.A., Bennai, R. (2024). Investigating wave propagation in sigmoid-FGM imperfect plates with accurate quasi-3D HSDTs. Steel and Composite Structures, 51(2), 185-202. https://doi.org/10.12989/scs.2024.51.2.185
31. Rafiee, M., Liu, X., He, X., Kitipornchai, S. (2014). Geometrically nonlinear free vibration of shear deformable piezoelectric carbon nanotube/fiber/polymer multiscale laminated composite plates. Journal of Sound and Vibration, 333(14), 3236-3251. https://doi.org/10.1016/j.jsv.2014.02.026
32. Reddy, J.N. (2003). Mechanics of laminated composite plates and shells: Theory and analysis (2nd ed.). CRC Press. https://doi.org/10.1201/9780203911164
33. Rad, A.B., Jafari, M. (2020). Hygroelasticity analysis of an elastically restrained functionally graded porous metamaterial circular plate resting on an auxetic material circular plate. Applied Mathematics and Mechanics, 41(9), 1359-1380. https://doi.org/10.1007/s10483-020-2644-9
34. Shen, H.S. (2009). A comparison of buckling and postbuckling behavior of FGM plates with piezoelectric fiber reinforced composite actuators. Composite Structures, 91(3), 375-384. https://doi.org/10.1016/j.compstruct.2009.06.007
35. Shi, X., Hassanzadeh-Aghdam, M., Ansari, R. (2021). A comprehensive micromechanical analysis of the thermoelastic properties of polymer nanocomposites containing carbon nanotubes with fully random microstructures. Mechanics of Advanced Materials and Structures, 28(4), 331-342. https://doi.org/10.1080/15376494.2019.1629055
36. Sun, R., Li, L., Zhao, S., Feng, C., Kitipornchai, S., Yang, J. (2021). Temperature-dependent mechanical properties of defective graphene reinforced polymer nanocomposite. Mechanics of Advanced Materials and Structures, 28(10), 1010-1019. https://doi.org/10.1080/15376494.2019.1624231
37. Tahir, S.I., Tounsi, A., Chikh, A., Al-Osta, M.A., Al-Dulaijan, S.U., Al-Zahrani, M.M. (2021). An integral four-variable hyperbolic HSDT for the wave propagation investigation of a ceramic-metal FGM plate with various porosity distributions resting on a viscoelastic foundation. Waves in Random and Complex Media, 31(5), 1-24. https://doi.org/10.1080/17455030.2021.1926569
38. Thostenson, E.T., Li, W.Z., Wang, D.Z., Ren, Z.F., Chou, T.W. (2002). Carbon nanotube/carbon fiber hybrid multiscale composites. Journal of Applied Physics, 91(9), 6034-6037. https://doi.org/10.1063/1.1466880
39. Yan, G., Zhou, X., El-Meligy, M.A., Sharaf, M. (2023). Nonlinear vibration analysis of graphene platelets reinforced nanocomposite doubly curved concrete panels subjected to thermal shock: Development of an artificial intelligence technique. Mechanics of Advanced Materials and Structures, 30(24), 1-22. https://doi.org/10.1080/15376494.2022.2105417
40. Yang, W., Yan, G., Awwad, E.M., Al-Razgan, M. (2023). AI-based solution on the efficient structural design of the graphene-platelets reinforced concrete ceilings. Mechanics of Advanced Materials and Structures, 30(24), 1-24. https://doi.org/10.1080/15376494.2023.2272179
41. Yuan, K.S., Deng, C.C., Wang, X.X., Li, Y.C., Zhou, C., Zhao, C.R., Dai, X.Z., Khan, A.R., Zhang, Z., Guidoin, R. (2025). Research advances and future perspectives of zinc-based biomaterials for additive

manufacturing. Rare Metals, 44(7), 4376-4410. https://doi.org/10.1007/s12598-024-03205-7
42. Zhang, B., Yu, J., Zhang, X. (2020). Guided wave propagation in functionally graded one-dimensional hexagonal quasi-crystal plates. Journal of Mechanics, 36(6), 773-788. https://doi.org/10.1017/jmech.2020.35